Ultrahigh-resolution seismic reflection imaging of the Alpine Fault, New Zealand

A. E. Kaiser,[1] A. G. Green,[1] F. M. Campbell,[1] H. Horstmeyer,[1] E. Manukyan,[1] R. M. Langridge,[2] A. F. McClymont,[3] N. Mancktelow,[4] M. Finnemore,[5] and D. C. Nobes[5]

Received 29 January 2009; revised 8 July 2009; accepted 31 July 2009; published 11 November 2009.

[1] High-resolution seismic reflection surveys across active fault zones are capable of supplying key structural information required for assessments of seismic hazard and risk. We have recorded a 360 m long ultrahigh-resolution seismic reflection profile across the Alpine Fault in New Zealand. The Alpine Fault, a continental transform that juxtaposes major tectonic plates, is capable of generating large (M > 7.8) damaging earthquakes. Our seismic profile across a northern section of the fault targets fault zone structures in Holocene to late Pleistocene sediments and underlying Triassic and Paleozoic basement units from 3.5 to 150 m depth. Since ultrashallow seismic data are strongly influenced by near-surface heterogeneity and source-generated noise, an innovative processing sequence and nonstandard processing parameters are required to produce detailed information on the complex alluvial, glaciofluvial and glaciolacustrine sediments and shallow to steep dipping fault-related features. We present high-quality images of structures and deformation within the fault zone that extend and complement interpretations based on shallow paleoseismic and ground-penetrating radar studies. Our images demonstrate that the Alpine Fault dips 75°–80° to the southeast through the Quaternary sediments, and there is evidence that it continues to dip steeply between the shallow basement units. We interpret characteristic curved basement surfaces on either side of the Alpine Fault and deformation in the footwall as consequences of normal drag generated by the reverse-slip components of displacement on the fault. The fault dip and apparent ~35 m vertical offset of the late Pleistocene erosional basement surface across the Alpine Fault yield a provisional dip-slip rate of 2.0 ± 0.6 mm/yr. The more significant dextral-slip rate cannot be determined from our seismic profile.

Citation: Kaiser, A. E., A. G. Green, F. M. Campbell, H. Horstmeyer, E. Manukyan, R. M. Langridge, A. F. McClymont, N. Mancktelow, M. Finnemore, and D. C. Nobes (2009), Ultrahigh-resolution seismic reflection imaging of the Alpine Fault, New Zealand, *J. Geophys. Res.*, *114*, B11306, doi:10.1029/2009JB006338.

1. Introduction

[2] Knowledge of fault zone structure in the shallow subsurface is important for understanding seismic hazard and risk. Key physical properties of potentially active faults are usually determined or inferred from surface outcrops, geomorphology, shallow boreholes, and/or trenches. High-resolution geophysical imaging at greater depths can extend and enhance interpretations of fault zone structure and behavior.

[3] The Alpine Fault is an example of a continental transform fault juxtaposing major tectonic plates. Similar in structure and tectonics to the well-known San Andreas Fault, it is a large transpressional strike-slip fault that accommodates much of the 36 mm/yr relative plate motion across the South Island of New Zealand. Although surface rupture of the fault has not been recorded in the ~200 years of European settlement, paleoseismic evidence suggests the fault is likely to rupture in large events (M > 7.8), posing a considerable seismic hazard in the region [*Sutherland et al.*, 2007].

[4] At our survey site along the northern section of the Alpine Fault (Figure 1), the fault trace emerges from dense bush and mountainous terrain to cross an open, relatively flat area known as Calf Paddock. Abandoned late Quaternary river terraces and stream channels formed by the Maruia River are offset vertically and horizontally across the main trace of the fault [*Wellman*, 1952], indicating ongoing displacement. Paleoseismic trenching suggests the last surface rupture at Calf Paddock occurred between 1530 and 1700 A.D. [*Yetton*, 2002]. Extensive 3D ground-

[1]Institute of Geophysics, Department of Earth Sciences, ETH Zürich, Zürich, Switzerland.
[2]GNS Science, Lower Hutt, New Zealand.
[3]Department of Geoscience, University of Calgary, Calgary, Alberta, Canada.
[4]Geological Institute, Department of Earth Sciences, ETH Zürich, Zürich, Switzerland.
[5]Department of Geological Sciences, University of Canterbury, Christchurch, New Zealand.

0148-0227/09/2009JB006338$09.00

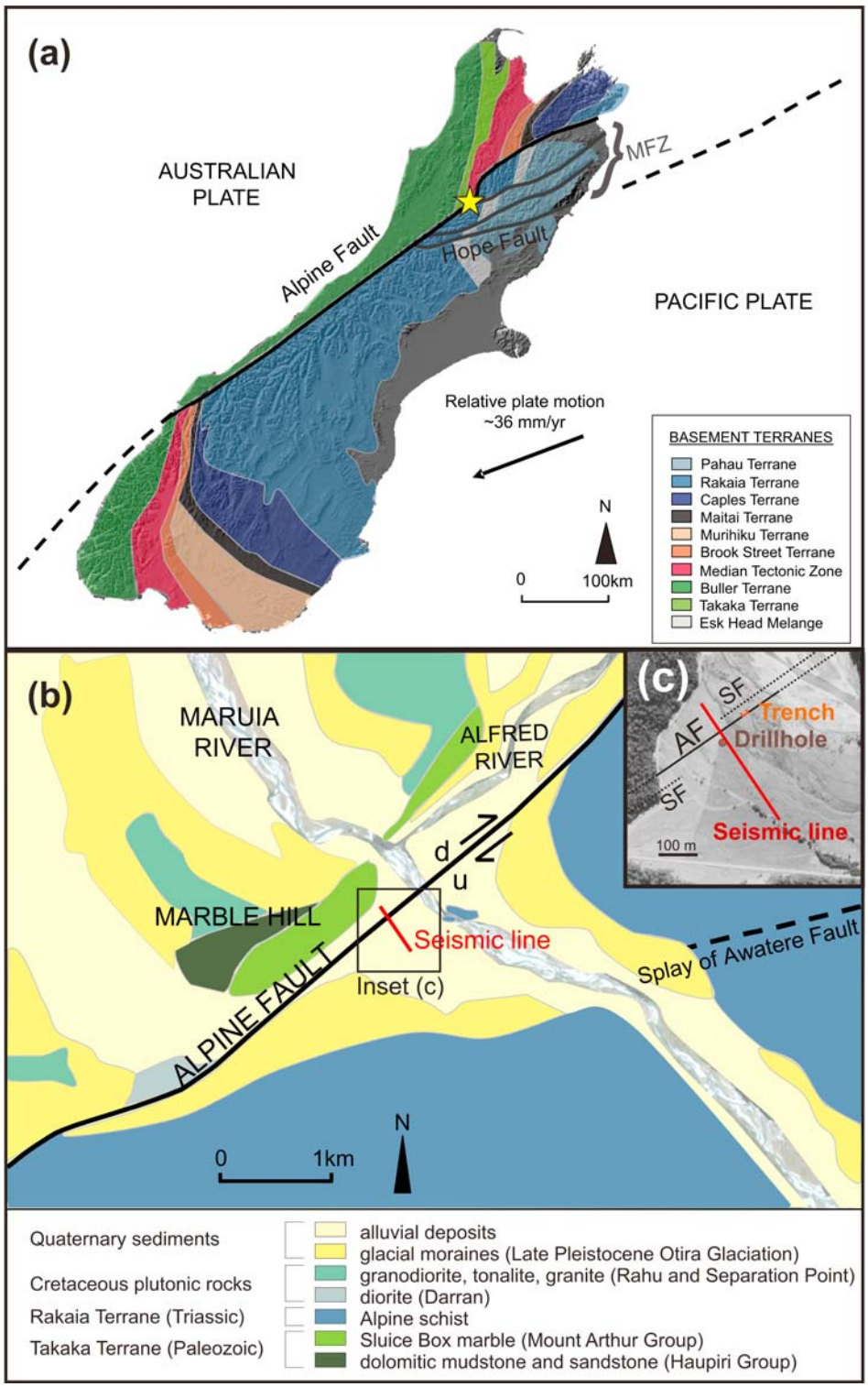

Figure 1. (a) Pre-Cenozoic basement terranes of the South Island of New Zealand (following the classification of *Bradshaw* [1989]) are offset by ~470 km along the Alpine Fault (black line). Much of the relative motion between the Australian and Pacific plates [*DeMets et al.*, 1994] in the north of the Island is taken up along the Alpine Fault and the Marlborough Fault Zone (MFZ). Continuations of the plate boundary offshore are marked by dashed lines. The yellow star indicates the location of our Calf Paddock study site. (b) Sketch of the local geology in the vicinity of the study area adapted from *Mabin* [1983] and *Nathan et al.* [2002]. (c) Aerial photograph of Calf Paddock showing the location of the seismic profile, borehole, and paleoseismic trench. Also shown are the Alpine Fault (AF, solid line where there is a visible surface scarp) and overlapping en echelon fault strands (SF) with no surface expression [*McClymont et al.*, 2009].

penetrating radar (GPR) surveys [*McClymont et al.*, 2008, 2009] delineate multiple fault strands in shallow Quaternary gravels, and a borehole and seismic refraction profiles [*Garrick and Hatherton*, 1974] provide limited constraints on fault geometry to basement depth. Detailed shallow geophysical imaging to the level of the basement and deeper has not previously been undertaken at Calf Paddock or elsewhere along the Alpine Fault.

[5] Imaging of shallow features presents general challenges for seismic processing that are amplified when the targets are complexly deformed structures associated with active fault zones [e.g., *Pratt et al.*, 1998; *McBride and Nelson*, 2001; *Improta and Bruno*, 2007]. Specific problems related to fault zones within unconsolidated sediments and underlying basement include (1) high degrees of near-surface heterogeneity (e.g., large lateral variations in near-surface velocity and weathered layer thickness) that require the careful computation and application of static corrections; (2) the presence of substantial source-generated noise (e.g., ground roll, guided phases, and multiple reflections); and (3) difficulties in imaging steeply dipping and/or severely deformed structures within and about the fault zone.

[6] Steeply dipping faults inferred from abrupt terminations or offsets of sedimentary reflections may be difficult to trace through less reflective basement unless reflections from the actual fault planes are recorded. However, there are only a few examples of reflections being recorded from steeply dipping strike-slip fault planes [*Lemiszki and Brown*, 1988; *Adam et al.*, 1992; *Stern and McBride*, 1998; *Hole et al.*, 2001; *Okaya et al.*, 2007].

[7] We have acquired ultrahigh-resolution seismic reflection data targeting shallow deformation structures in the Alpine Fault zone down to and beyond basement depth. With careful processing and interpretation we have addressed many of the problems inherent in the high-resolution seismic imaging of active faults. Our final high-quality seismic images have provided constraints on key physical properties of the shallow fault zone at Calf Paddock.

[8] After describing the geological setting and seismic data acquisition, we outline our processing strategies with emphasis on the calculation and application of corrections for near-surface velocity heterogeneity and enhancement of very shallow reflections. Stacked and migrated sections then reveal conspicuous offsets in basement reflections and ambiguous moderately steep dipping ($\sim$50°) energy near the projected location of the fault zone within the basement. We use a finite element modeling approach to investigate the origin of the moderately steep dipping energy in Appendix A. Finally, we discuss the significance of these features and present a provisional geological interpretation of the migrated seismic section.

2. Alpine Fault

2.1. Variation in Slip Rates

[9] The Alpine Fault marks the boundary between the Australian and Pacific plates through the South Island of New Zealand (Figure 1a). It is a major transpressive dextral fault that accommodates approximately two thirds of the relative plate motion [*Sutherland et al.*, 2006; *Norris and Cooper*, 2007]. Basement terranes are laterally offset > 470 km across the fault, and a smaller but important component of convergence is responsible for rapid uplift of the Southern Alps. Maximum dextral and dip-slip rates of $\sim$25 mm/yr and 10 mm/yr occur along the central section of the fault [*Berryman et al.*, 1992; *Norris and Cooper*, 2001]. To the north, relative plate motion is increasingly taken up by younger strike-slip faults of the Marlborough Fault zone (MFZ in Figure 1a), such that the estimated slip on the Alpine Fault decreases north of the intersection with the Hope Fault to $\sim$10 mm/yr (dextral) and $\sim$6 mm/yr (dip slip) [*Norris and Cooper*, 2001; *Langridge and Berryman*, 2005]. Further north at our survey site, the slip rates are likely to have decreased further, though this has not been quantified.

2.2. Variations in Fault Character

[10] Much of the Alpine Fault appears as a simple linear trace striking 055° on satellite photos [*Berryman et al.*, 1992]. It is inferred to have a moderate to steep southeasterly dip through the upper crust [*Norris and Cooper*, 2007]; reflections at $\sim$20 – 30 km depth on regional-scale seismic reflection profiles east of the Alpine Fault have been interpreted as defining a fault plane dipping $\sim$50° to the east [*Davey et al.*, 1995; *Kleffmann et al.*, 1998; *Okaya et al.*, 2007]. At shallower depths, oblique slip is accommodated through more complex fault structures. In the central section of the Alpine Fault, the surface trace follows a zigzag pattern of alternating predominantly strike-slip and predominantly thrust sections on a scale of 1–10 km [*Norris and Cooper*, 1995]. Steeply dipping narrow fault zones are inferred along the strike-slip sections, whereas relatively shallow fault dips have been observed at outcrops of the thrust sections. Further north toward our study site, the fault trace appears roughly linear with small scale en echelon step overs [*Berryman et al.*, 1992], suggesting that oblique slip is accommodated differently in this region. Additional detailed imaging of the near-surface fault zone at Calf Paddock to elucidate questions of fault dip and geometry as well as the nature of near-surface faulting is therefore of interest.

2.3. Local Geology

[11] At Calf Paddock (Figure 1b), the Alpine Fault is distinguished by a $\sim$2 m high linear fault scarp that cuts across a sequence of abandoned terraces of the Maruia River. The constituent glaciofluvial valley sediments date from periods of late Pleistocene aggradation that followed phases of advance and retreat of the Maruia Glacier [*Suggate*, 1965; *Mabin*, 1983]. During the last phase of ice advance (i.e., the end of the late Pleistocene Otira Glaciation, c. 22–14 ka), the glacier flowed from the southeast dividing into two lobes on either side of Marble Hill (Figure 1b) [*Mabin*, 1983]. Basement southeast of the fault is Triassic age Alpine schist, whereas that to the northwest is locally variable with Paleozoic age marble outcropping close to our seismic profile [*Nathan et al.*, 2002].

[12] Paleoseismic trenches 60–80 m to the northeast of our seismic profile on the youngest river terrace intercept a narrow zone of variably dipping (40°–90°) faults within the upper 1–2 m of gravels [*Yetton*, 2002]. Such gravels are either exposed at the surface or covered by a thin layer of undisturbed topsoil. GPR surveys at Calf Paddock reveal a

Table 1. Data Acquisition Parameters

Parameter	Details
Source	5 kg hammer (6 stacked blows)
Geophone frequency	30 Hz
Receiver spacing	0.5 m
Source spacing	1 m
Lateral offset of source	0.5 m
CMP spacing	0.25 m
Fold	~60
Source-receiver offset range	typically 0.5–60 m
Active channels	240
Line length	360 m
Record length	1500 ms
Sample rate	0.125 ms

narrow fault zone dipping steeply to the southeast at ~80° to a depth of ~15 m [*McClymont et al.*, 2008, 2009]. Notable changes in GPR reflection geometry are observed across the main strand of the fault. Additional changes in reflection characteristics ~30 m on either side of the main trace are interpreted as secondary left-stepping en echelon fault strands and associated deformation. GPR data allow one of these secondary fault strands to be mapped to within 30 m of our seismic profile (SF in Figure 1c). The relationships between the main fault and secondary faults below the sediment cover are unknown.

[13] *Garrick and Hatherton* [1974] describe the results of seismic refraction surveying along lines perpendicular and oblique to the fault. They also present information from a borehole 39 m southeast of the fault trace (Figure 1c) that penetrated 26 m of gravels and underlying basement schist to a depth of 83 m. The borehole revealed zones of shearing and a steeply dipping fault within the schist, but it did not reach the Alpine Fault itself. Interpolating from the surface scarp to the basement offset (inferred from the refraction profiles) and the base of the borehole led them to estimate a minimum average fault dip of ~65° at this location.

[14] The strong change in lithological and seismic properties at the sediment-basement contact observed in the borehole and refraction data correlate well with the strongest reflections in our data. We interpret this contact to represent an unconformity formed by glacial erosion during the late Pleistocene. Subsequent offset and deformation of this important marker surface is highlighted in our seismic images.

3. Ultrahigh-Resolution Seismic Data Acquisition

[15] Our ultrahigh-resolution seismic data were acquired along a line oriented perpendicular to the surface fault scarp, approximately 10 m northeast of a fault-monitoring concrete wall that acts as a large strain gauge. Evison's Wall, erected at the site in the 1960s, is now a well-known New Zealand landmark. Acquisition parameters (Table 1) were chosen to provide highly detailed images of the fault zone from the near-surface through the Quaternary sediments and basement to depths of ~150 m. A 5 kg hammer source (six blows against a steel plate) located every 1 m along the profile provided adequate depth penetration and a broad frequency bandwidth of reflection energy. Stacking seismic signals generated by the hammer blows increased the signal-to-ambient-noise ratio and reduced the relative strength of the recorded steel plate 'bounce' at traveltimes > 100 ms.

[16] Data were recorded on a 240-channel 24-bit Geometrics Geode acquisition system. Receivers (single vertical 30 Hz geophones) spaced at 0.5 m intervals were offset from the sources by ~0.5 m to the southwest. Roll-along was achieved by moving 48 receivers at a time. The resulting 360 m long profile has a fold of up to 60 with a common midpoint spacing of 0.25 m.

4. Seismic Data Processing

[17] Careful processing (Table 2) was required to produce meaningful images of the Alpine Fault and adjacent regions. Although the individual processes in Table 2 are relatively standard tools in deep exploration seismology, it was necessary to adapt the processing flow and parameters to address the specific problems of our complex shallow data set. To ensure that all critical events were preserved and that artificial reflections were not created, it was essential to follow the results of the testing and processing on representative common source and common midpoint (CMP) gathers and stacks of the data [*Steeples et al.*, 1997; *Büker et al.*, 1998]. Such an approach was especially important in our attempts to image ultrashallow (<10 m depth) structures [*Schmelzbach et al.*, 2005]. Each process was eventually applied on the basis of demonstrated clear overall improvement of the unmigrated and migrated images. We present (1) the results of our general processing sequence, (2) a

Table 2. Data Processing Scheme

Scheme	Details
Standard Processing	
Prestack	
Trace editing	
Time-variant spectral whitening	10 ms: 100-120-500-600 Hz
	100 ms: 100-120-450-550 Hz
	250 ms: 100-120-400-500 Hz
AGC	Window length 80 ms
Refraction statics	Two-layer model with static solution based on an iterative delay-time method
Residual statics	Max. power surface-consistent solution
Airwave attenuation	Attenuation of energy at 334 m/s
	Offsets 0 – 40 m: window width 6 ms
	Offsets > 40 m: window width 16 ms
Top mute	Hand-picked top mutes
F-K filtering	Pass velocities > 350 m/s
Velocity analysis	
NMO correction	Stretch mute 50 %
CMP stacking	
Poststack	
F-X deconvolution	Time window 80 ms
	Horizontal window 12 traces
	No. of filter samples 7
Band-pass filter	100-120-500-600 Hz
Phase shift time migration	Up to 90° dip
	100 % smoothed interval velocity field
Depth conversion	Smoothed interval velocity field
Alternative Processing to Enhance Shallow Reflections	
Surface-consistent spiking deconvolution[a]	Operator length 60 ms
Band-pass filter[a]	100-120-500-600 Hz
Ground roll mute[a]	Hand-picked bottom mute
DMO	Dip-scan stack method

[a]These three processes replace spectral whitening in the standard processing scheme.

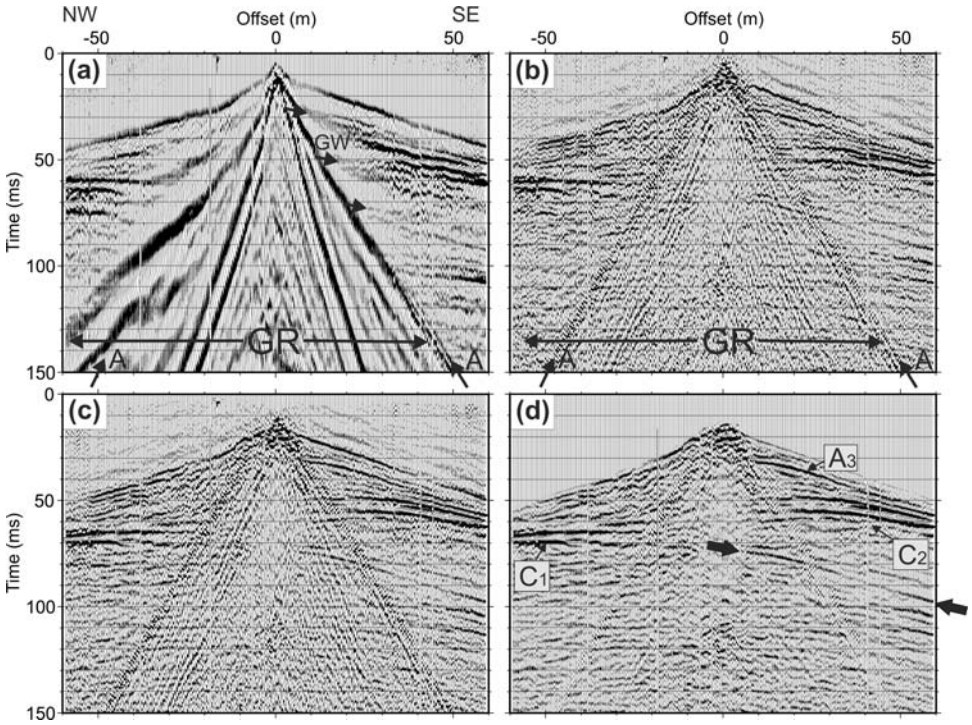

Figure 2. Results of processing applied to a typical source gather. (a) Raw source gather with an 80 ms AGC for display purposes illustrating noise contamination by ground roll (GR), guided phases (GW) and air wave (A). (b) Same as Figure 2a with application of time-variant spectral whitening prior to 80 ms AGC. (c) Same as Figure 2a with application of refraction and residual-static corrections (to intermediate datum for display purposes). (d) Same as Figure 2a after F-K filtering, muting of first breaks, and air wave attenuation. Major reflections from within the Quaternary sediments (A3) and from the offset basement on either side of the fault (C1, C2) are identified. Diffraction from the termination of reflector C1 is marked by arrows.

near-surface tomographic velocity model that helps us devise an appropriate strategy for determining static corrections, and (3) the output of an alternative processing sequence designed to enhance the shallowest reflections from the Quaternary sediments.

4.1. Prestack Processing

[18] Raw source gathers (e.g., Figure 2a) are dominated by low-frequency (<140 Hz, peak frequency ~50 Hz) ground roll and higher frequency air waves. In many source gathers, strong low-frequency guided phases are also present, representing trapped energy within the near-surface low-velocity layer [e.g., *Robertsson et al.*, 1996]. Strong reflections are visible only within the optimum reflection windows. Spectral analysis shows that reflections generally have a broad bandwidth of up to 600 Hz with a peak frequency of ~150 Hz. As a consequence, they can be separated in the frequency domain from the ground roll and guided phases to a large degree. Spectral whitening in the range 100–600/500 Hz successfully removes much of the coherent noise and sharpens the reflections (Figure 2b). A time-variant spectral whitening scheme is adopted, in which the maximum frequency is reduced with increasing traveltime to avoid amplifying high-frequency noise with depth (Table 2).

[19] Large static shifts in the data were caused by topographic relief (up to 5 m; our shallowest targets are only 3.5 m below the surface at some locations) and strong lateral variations in the properties of the near-surface weathering layer. After applying refraction-static corrections, which are discussed in some detail in the next section, we accounted for small residual-static shifts using a method that maximizes the CMP stack power within selected windows and chosen source-receiver offset ranges [*Ronen and Claerbout*, 1985]. Strict quality control and testing of the residual static solutions were necessary; clearly erroneous values were identified and removed. A first pass of residual static computation and application (source/receiver corrections < 0.6 ms) was followed by renewed velocity analyses and a second residual static calculation (corrections < 0.3 ms). Application of surface-consistent refraction and residual static corrections markedly enhanced the coherency and stacking power of reflections (Figure 2c).

[20] Airwave attenuation, mild F-K filtering, and a top mute reduced remaining coherent noise (Figure 2d) before stacking. The F-K filter was designed to pass coherent events with apparent velocities > 350 m/s, thus attenuating residual surface wave energy while enhancing the coherency of reflections. This filter was most effective in the source domain, because the close trace spacing (0.5 m) allowed filtering of higher frequencies without introducing artifacts due to aliasing.

4.2. Refraction Tomogram and Computation of Refraction Static Corrections

[21] First-arrival traveltimes in source gathers (e.g., Figure 3a) provide evidence for considerable velocity con-

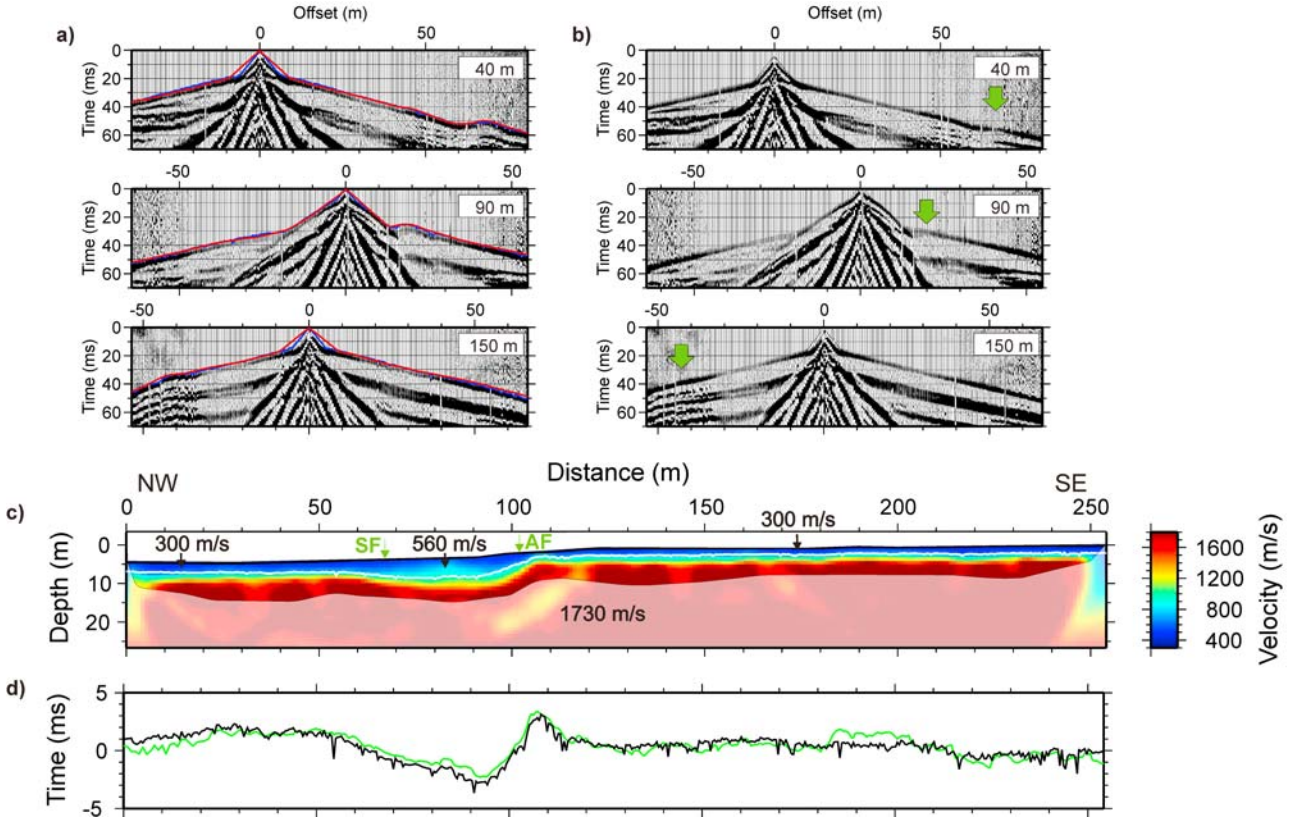

Figure 3. (a) Example source gathers at 40, 90, and 150 m distance along the profile with picked first arrivals (blue line) and modeled first arrivals based on refraction tomographic inversion (red line, which mostly overlies the blue line). (b) Source gathers as in Figure 3a after application of final refraction static corrections. Arrows highlight reductions in first-arrival undulations near the location of the surface scarp. (c) Comparison of the refraction tomogram (color plot; bold colors indicate areas of good ray coverage) and a simple refraction static velocity model based on a two-layer iterative delay time method (white line and representative velocities shown by black numbers) along a section of the seismic profile. Also marked are the locations of the main Alpine Fault trace (AF) and the projected location of the left-stepping en echelon fault strand SF identified in 3D GPR data [*McClymont et al.*, 2009]. (d) Source (green) and receiver (black) refraction-static corrections to the intermediate datum determined from the delay time method.

trasts and lateral variations in the near-surface weathering layer. By modeling this layer via a tomographic inversion of first arrivals, we demonstrate that a simple two-layer velocity model for refraction-static calculations is appropriate. We show that failing to adequately correct for near-surface velocity variations can lead to erroneous stacking of reflections.

[22] A semiautomated picking algorithm was used to estimate first-arrival traveltimes on all source gathers. Subsequent minor manual corrections were necessary for near and long offsets and noisy traces. In general, errors in picks were estimated to be <1.5 ms. Errors may have been greater at near offsets, where direct arrivals and airwaves overlapped to some degree.

[23] We employed a tomographic algorithm based on a fast finite difference Eikonal solver for calculating 2D raypaths and traveltimes and a least squares scheme for the inversion [*Lanz et al.*, 1998]. Our simple 1D starting model had a velocity of 100 m/s at zero depth that increased linearly to 2200 m/s at 40 m depth and a strongly reduced gradient thereafter. Weights for data (45.5%), smoothing (45.5%), and damping (9%) in the inversion process were chosen on the basis of systematic trial inversions and a qualitative trade-off analysis of model complexity and root-mean-square (RMS) deviation between the observed and model-predicted traveltimes. An RMS deviation of 1.3 ms was obtained after 15 iterations; this deviation is close to the <1.5 ms first-break picking errors. Model-predicted traveltimes in Figure 3a closely match the picked values at most offsets. Some overestimation of the velocity occurs for near-offset traces, where the inversion struggles to fit the strong near-surface velocity gradient.

[24] Tests show that the results of the inversion are robust, with the main features of the velocity tomogram in Figure 3c being relatively insensitive to the choice of starting model and regularization parameters. For the processing of the seismic reflection data, the near-surface low-velocity layer (shown by the blue to yellow colors in Figure 3c) is the most important feature in the velocity tomogram. Large source and receiver static shifts of up to 3 ms result from its changing velocity and thickness; a combination of simple

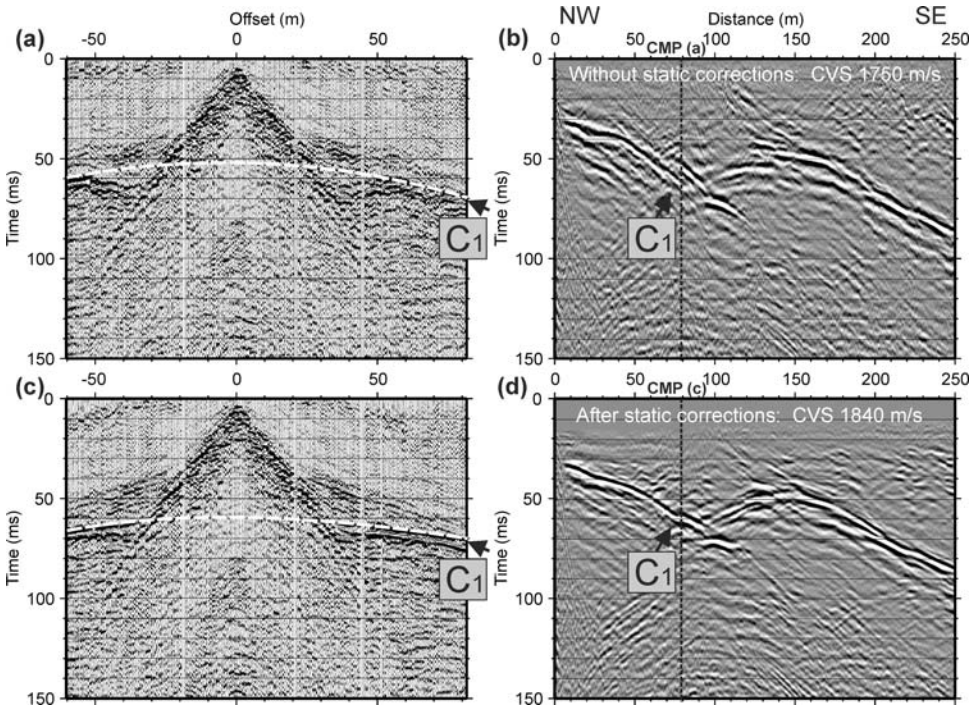

Figure 4. (a) Example processed CMP supergather with no static corrections applied. Reflection C_1 is distorted by severe static problems and stacks at an anomalously low velocity defined by the best fit hyperbolic path (white line). (b) Part of equivalent constant-velocity stack. At location of CMP gather (Figure 4a), reflection C_1 appears offset by >10 ms. (c and d) Same as Figures 4a and 4b after application of refraction and residual static corrections. Reflection C_1 now stacks with an appropriate velocity and the apparent reflection offset in the stack is significantly reduced.

elevation and residual static corrections do not correct for such shifts.

[25] A two-layer refraction static velocity model appears to be appropriate for our data (Figure 3c). We use weathering layer velocities estimated from the direct arrivals along the length of the line and initial smoothed refractor velocities to determine refractor depth and source and receiver delay times through iterative inversion (based on the work by *Lawton* [1989]). The resulting simplified refraction static velocity model reflects the main features imaged in the velocity tomogram (Figure 3c). Source and receiver refraction static corrections to an intermediate datum above the topography are then calculated using a replacement velocity of 1730 m/s. Application of the computed static corrections (Figure 3d) to source gathers substantially reduces the distortion of phases across the fault (compare traces marked by green arrows in Figure 3b with the equivalent traces in Figure 3a).

4.3. Application of Refraction and Residual Static Corrections

[26] The combination of refraction- and residual-static corrections improves the coherency of stacked reflections and reduces stacking artifacts due to nonhyperbolic reflection moveout. Severe static problems are apparent in CMPs centered above the thickest part of the low-velocity layer (distances 60–105 m in Figure 3c). In the example CMP supergather of Figure 4a, the strong reflection C_1 is obscured at near offsets by surface wave energy. At offsets > 30 m, the reflection is distorted by progressive thinning of the low-velocity layer, such that maximum stacking power occurs along an incorrect hyperbolic path and the reflection appears discontinuous when stacked (Figure 4b). Correction of near-surface effects using the combined refraction and residual static corrections improves the coherency in the CMP domain (Figure 4c) and eliminates the artificial discontinuity of reflection C_1 in the stack (Figure 4d). In cases such as this, underestimating the effects of near-surface lateral velocity variations when calculating static corrections would lead to structural misinterpretations.

4.4. Velocity Analysis and Poststack Processing

[27] Stacking velocities (Figure 5) were determined from careful analyses of constant-velocity stacks and semblance plots. Velocities ranged from 1580–1700 m/s for the deeper Quaternary sediments (A and B units) to 1750–2500 m/s for the dipping sediment-basement interface (C reflections) and deeper features. Where events had conflicting dips (e.g., B and C_2 at 95 – 110 ms; Figure 5b), compromise velocities were chosen from the constant-velocity stacks to image the most important structural features. Application of dip moveout corrections to this data set did not improve the imaging of all events with conflicting dips, and even weakened some strongly dipping deeper features (e.g., diffractions).

[28] F-X deconvolution [*Canales*, 1984; *Yilmaz*, 2001] and band-pass frequency filtering enhanced the signal-to-noise ratio after stack (Figure 6a). Phase shift time migration using a smoothed interval velocity field was then

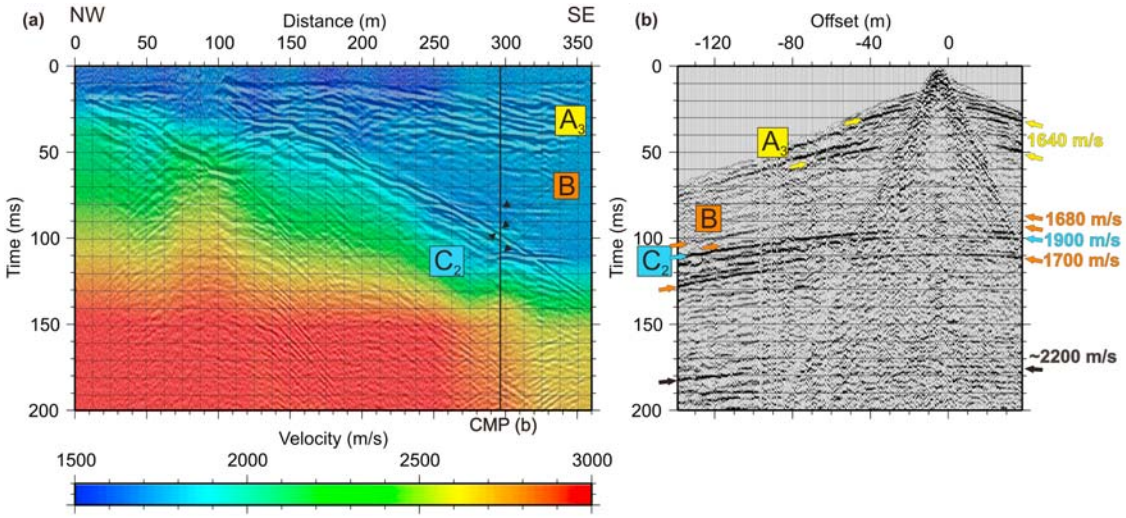

Figure 5. (a) Unmigrated stack and stacking velocities. (b) Processed CMP supergather corresponding to location shown in Figure 5a. Important reflections are highlighted and color-coded to seismic units A_3, B, and C_2. Note that the data are shifted to a floating datum for velocity analysis.

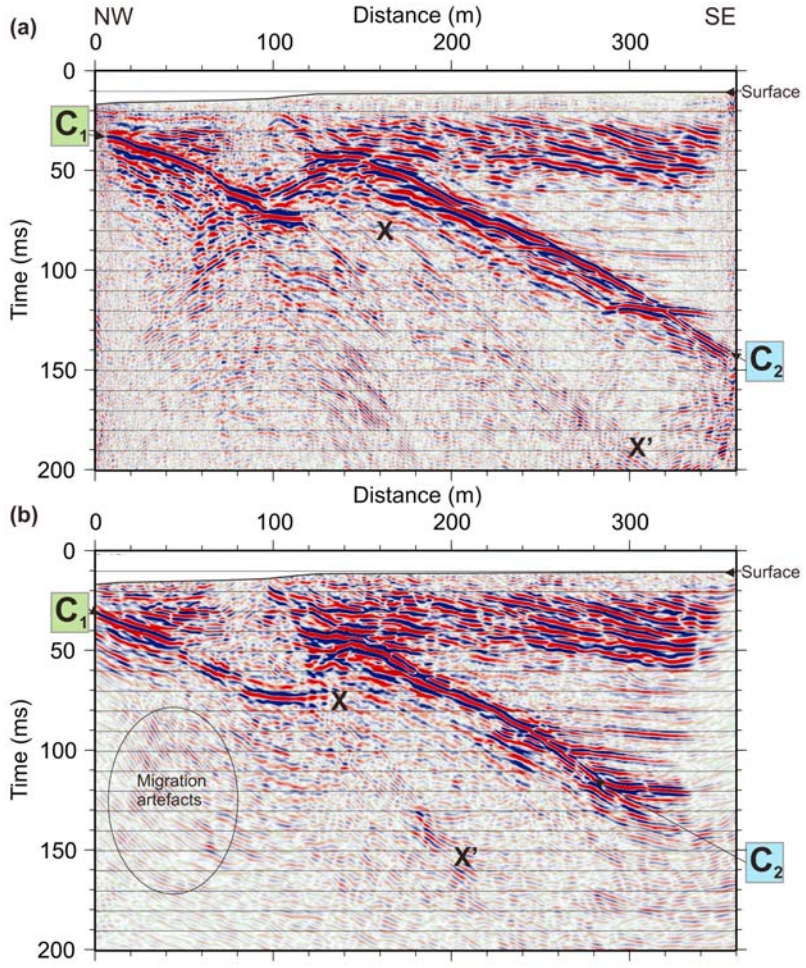

Figure 6. (a) Unmigrated and (b) phase shift time-migrated stacks. Diffractions collapse and reflections move to their true subsurface positions after migration, resulting in a clearer image. Key reflections C_1 and C_2, and the weak energy band X-X′ are marked. Fine line at the top of the section delineates the surface after replacing the low-velocity weathering layer with 1730 m/s material. Dark blue shading represents positive pulse polarity.

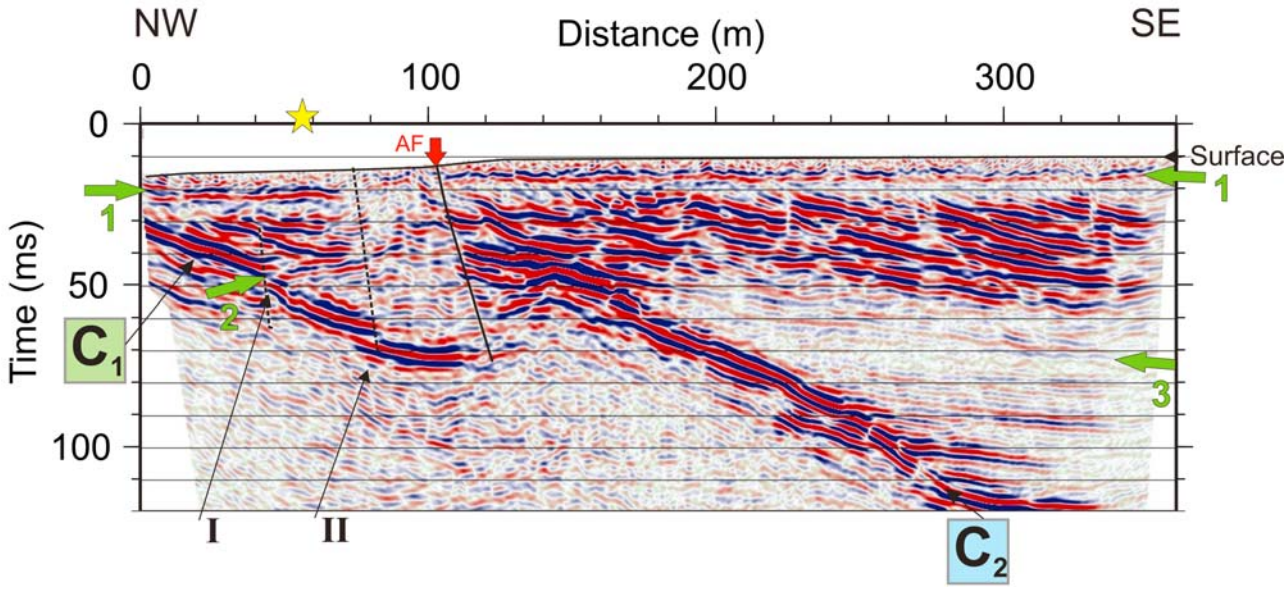

Figure 7. Migrated stack after alternative processing designed to image the shallowest reflections (Table 2). Note the improved continuity and sharpness of shallow reflections 1–3 marked by arrows (compare to Figure 6b). Traces of the Alpine Fault AF (solid line) and faults I and II in the footwall (dashed lines) are inferred from abrupt changes in reflection patterns. Location of the source gather shown in Figure 8 is marked by the star. Fine line at the top of the section delineates the surface after replacing the low-velocity weathering layer with 1730 m/s material. Dark blue shading represents positive pulse polarity.

performed (based on the work by *Gazdag* [1978]). Phase shift migration was chosen to optimize the imaging of moderately to steeply dipping events, though other migration schemes (including depth migration) produced similar results. Diffractions from reflection terminations were successfully collapsed in the final migrated image (compare Figures 6a and 6b). Finally, time-to-depth corrections using a strongly smoothed interval velocity field were applied. Excellent agreement of the final depth-converted stack with borehole information ~39 m southeast of the fault trace was achieved by using 100% of the smoothed interval velocity field for migration and depth conversion.

4.5. Enhancing Shallow Features With Alternative Processing

[29] An alternative processing scheme (Table 2) was designed to improve the resolution of very shallow reflections and abrupt truncations and vertical offsets of reflections caused by steeply dipping faults (compare Figure 7 with Figure 6b). The alternative processes included surface-consistent deconvolution, bottom mutes, and dip-moveout corrections.

[30] Surface-consistent spiking deconvolution [*Levin*, 1989; *Yilmaz*, 2001], which replaced time-variant spectral whitening in our general processing flow, successfully enhanced shallow reflections inside the optimum reflection window; signal-to-noise ratios and reflection coherency were improved and near-surface reverberations (e.g., following C_2 in Figure 6b) were largely attenuated. Because strong surface wave energy remained outside this window, application of a significant bottom mute to the source gathers was necessary. Consequently, deeper reflections and diffractions best seen within the portions of source gathers affected by ground roll energy were not clearly imaged after deconvolution. Thus, spectral whitening was a more robust solution for the general processing of our data.

[31] Dip moveout corrections (DMO) using a dip scan stack technique [*Jakubowicz*, 1990] further enhances shallow reflection coherency. DMO techniques are traditionally employed to image events with conflicting dips, determine true stacking velocities of dipping events, and reduce reflection point smear. Only shallow reflections from the Quaternary sediments (e.g., 2 and 3 in Figure 7) are improved in this manner. In addition, DMO is principally responsible for the markedly enhanced image of the shallowest reflection (1 in Figure 7) in our data.

[32] Except for an offset that follows the change in topography at the Alpine Fault and an adjacent 30 m long disrupted zone to the northwest, the ultrashallow reflection 1 is relatively flat and continuous along the length of the profile. It originates from a discontinuity at 4.5–5 m depth to the northwest of the Alpine Fault (5–6 ms below the surface on the refraction static corrected section of Figure 7; for such shallow events, the replacement velocity of 1730 m/s converts traveltime to depth) and slightly shallower at ~3.5 m (~4 ms) to the southeast. This reflection is visible as a clear hyperbolic event with a low normal moveout (NMO) velocity of ~500 m/s in some CMP gathers (e.g., Figure 8). Generally, imaging ultrashallow events using standard processing schemes is problematic because of the large velocity gradients and resulting effects of NMO stretch. The dip scan stack DMO method successfully enhanced this low stacking velocity reflection without adversely affecting the image of deeper reflections.

[33] In addition to the large offset of basement reflection $C_1 - C_2$ at the Alpine Fault (AF in Figure 7), prominent

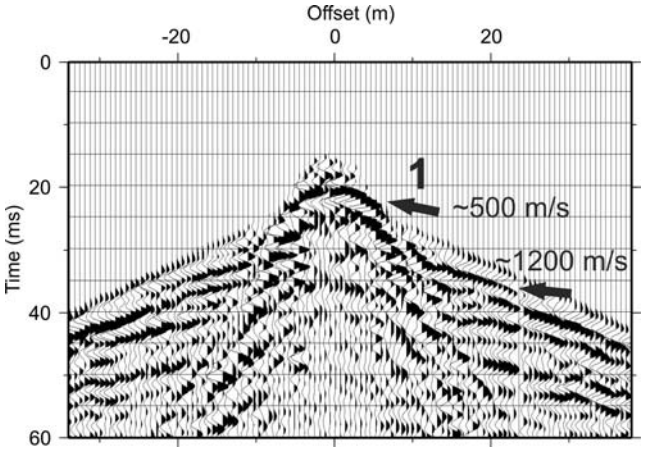

Figure 8. CMP supergather (location marked by star in Figure 7) showing ultrashallow reflection 1 at ~20 ms traveltime. Its ~500 m/s NMO velocity is significantly lower than the 1200 m/s NMO velocity of the reflection from the underlying sediments. Note that the data are shifted to the intermediate datum, such that the traveltime of reflection 1 corresponds to that shown in Figures 6 and 7.

vertical offsets I and II are observed in the footwall basement reflection C_1 at ~45 and ~80 m distance. At location II, reflection C_1 is clearly offset ~5 ms in source gathers (arrows in Figure 9), indicating a sharp ~5 m basement dislocation at this position. Although no clear offset is discerned in source gathers at location I, the unmigrated stack contains a conspicuous weakening and change in dip of reflection C_1 at the relevant position (Figure 6a). We conclude that there is a small fault at location II and a high probability of another at location I.

5. Geological Interpretation

[34] Our provisional interpretation of the ultrahigh-resolution seismic reflection data set acquired at Calf Paddock is based on the unmigrated section in Figure 6a and the migrated sections in Figures 6b, 7, and 10.

5.1. Ultrashallow Seismic Reflector/Refractor

[35] The depth and character of the boundary causing the ultrashallow reflection 1 at distances of 0–70 m and 100–360 m in Figure 7 matches the strong velocity gradient at the 1200 m/s isovelocity line (yellow line) in the tomogram of Figure 3c. This boundary could be the top of the groundwater table and/or a change in sediment facies. The estimated increase in velocity from 300–560 m/s above the boundary to more than 1700 m/s below is typical of a transition from dry to saturated sediments [*Telford et al.*, 1990], and the proximity of the Maruia River indicates that the groundwater table must lie in the depth range of our tomogram. However, the ~5 m step across the fault scarp, which is greater and sharper than the fault expression at the surface, and the slight thickening of the low-velocity layer to the northwest support an interpretation in terms of a sediment facies change. The contact between subhorizontally layered Holocene fluvial sediments of the Maruia River and underlying dipping late Pleistocene gravels is imaged in 3D GPR data at approximately the same depth as the seismic boundary [*McClymont et al.*, 2008, 2009] (the GPR data were collected during a wetter period when the groundwater table was close to the surface, such that it was not imaged in the GPR data). Taking all observations into account, we interpret the shallow boundary at 3.5–5 m depth as the groundwater table that is controlled to some degree by the contact between the Holocene and late Pleistocene gravels. The thickening of the low-velocity layer in the footwall of the fault at distances of 60–100 m likely results from an accumulation of sediment in a colluvial wedge at the base of the fault scarp.

5.2. Interpretation of Seismic Units

[36] We identify six distinct seismic units (A_1, A_2, A_3, B, C_1, C_2) on the migrated depth-converted section in Figure 10:

[37] 1. Seismic units A_1, A_2, and A_3 of strong semi-continuous reflections on either side of the fault from near the surface to as deep as ~60 m are interpreted to be late Pleistocene gravels. Undifferentiated gravel was intersected from the near surface to 26 m depth in the borehole southeast of the surface fault trace [*Garrick and Hatherton*, 1974]; note the good correlation between the thickness of gravels observed in the seismic image and the borehole information (Figure 10).

[38] 2. Reflections from seismic unit A_3 appear to grade into gently dipping continuous reflections B at greater depth. We interpret seismic unit B as layered sediments from an earlier period of less turbulent deposition.

[39] 3. The sediment-basement interface produces strong reflections C_1 and C_2 that are offset across the Alpine Fault and at other locations along the profile. From mapped surface outcrops (Figure 1b), we infer that marble basement C_1 to the northwest is juxtaposed against schist basement C_2 to the southeast.

[40] Extensive glaciation of the Maruia Valley occurred during the late Pleistocene Otira Glaciation. This incorporated five main phases of ice advance and retreat from ~22,000 to ~14,000 years before present [*Mabin*, 1983; *Suggate*, 1990]. The relatively smooth basement imaged in the seismic data is interpreted as an erosional surface that deepened toward the former valley floor during this period. This surface has enhanced curvature in the shallow part of

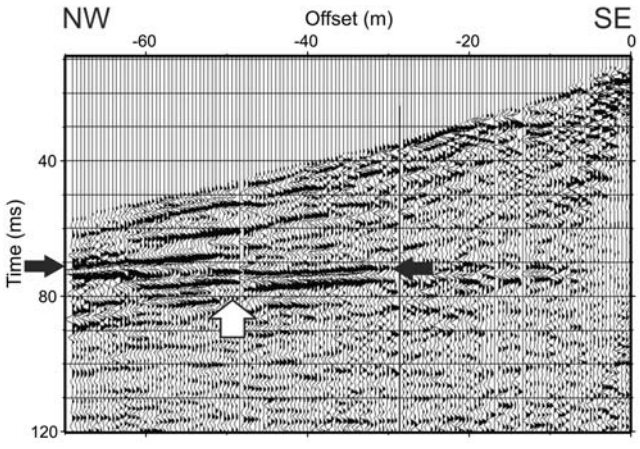

Figure 9. Offset basement reflection (black arrows) observed in a processed source gather. The location of the offset is shown by the white arrow.

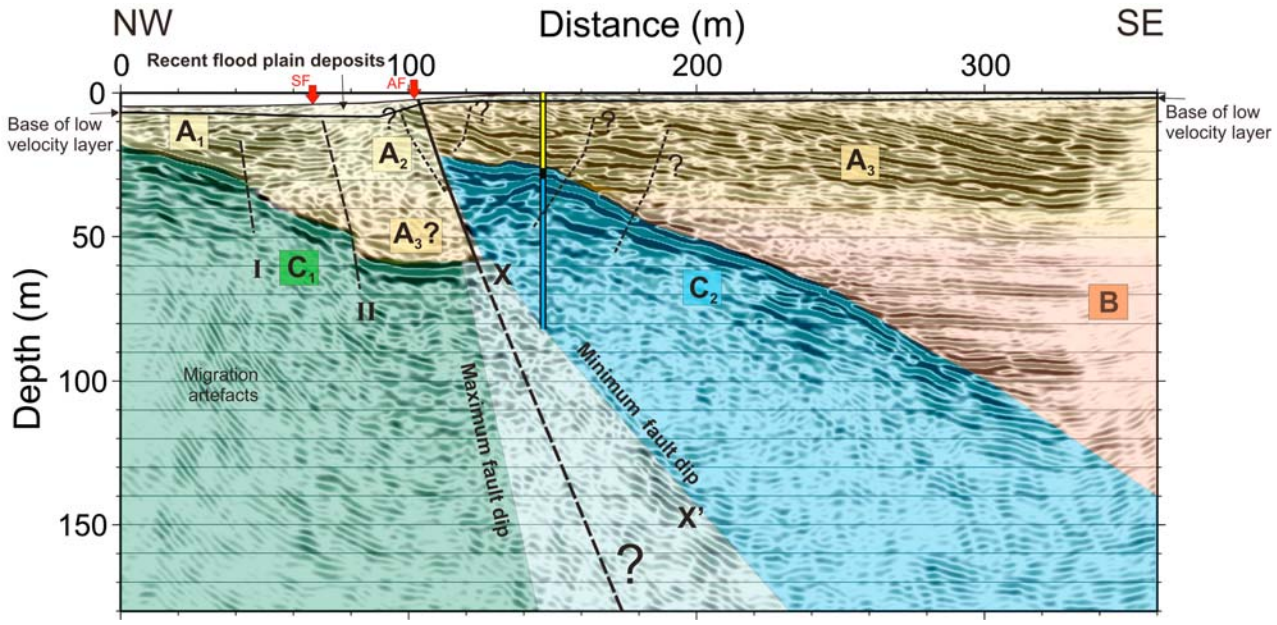

Figure 10. Interpretation of the depth-converted migrated section. The base of the low-velocity layer in the two-layer refraction-static velocity model of Figure 3c is shown by the thin line. Seismic units A_1, A_2, A_3, B, C_1, and C_2 are identified. Moderately steep dipping energy X-X′ is discussed in the main text and in Appendix A. The interpreted main trace of the Alpine Fault and inferred extension are marked by solid and dashed thick lines, respectively. Possible subsidiary faults, including those marked I and II, are also indicated by dashed lines. The borehole [*Garrick and Hatherton*, 1974] is shown projected onto the seismic profile (for location see Figure 1c). Red arrows mark the surface location of the main fault trace AF and the projected location of the left-stepping en echelon fault strand SF identified in 3D GPR data [*McClymont et al.*, 2009]. Relative to Figures 6b and 8, a 10 ms bulk shift has been applied to bring the zero-depth reference from the intermediate datum to the highest elevation along the profile.

the section, an apparent primary vertical offset of ~35 m, and two secondary vertical offsets of ~5 m, all of which we associate with subsequent transpressive movement along the Alpine Fault (AF in Figure 10) in the late Pleistocene and Holocene.

[41] The valley sediments are likely to originate from periods of late Pleistocene postglacial aggradation [*Suggate*, 1965; *Mabin*, 1983]. From their gently dipping layered geometry, older sediments of seismic unit B (>50 m thickness) are likely to be glaciolacustrine in origin. Younger sediments extending to the near surface (seismic units A_1, A_2, and A_3) were probably deposited in glaciolacustrine fan, alluvial, and/or glaciofluvial environments. Note the marked change in reflection pattern across the Alpine Fault.

[42] Characteristic seismic units A_1, A_2, and A_3 are mirrored in the higher resolution 3D GPR data [*McClymont et al.*, 2008, 2009]. Although the hanging wall seismic reflections A_3 have apparent dips of ~15° to the southeast (Figures 7 and 10), the 3D GPR data suggest the true dips are oblique to the profile and somewhat steeper at 20°–35° to the southwest. *McClymont et al.* [2009] interpret these sediments to result from progradation of a late Pleistocene alluvial or glaciolacustrine fan in a northeast to southwest direction. This fan likely extended across the fault and some distance further into the valley to the southwest, as suggested by the >40 m thickness of unit A_3. As a consequence, we infer the presence of similar fan sediments overlying the basement unconformity in the footwall and juxtaposed after lateral movement along the fault.

[43] Immediately to the northwest of the Alpine Fault and extending for about 30 m, reflections of footwall seismic unit A_2 have relatively low amplitudes and variable dips (Figures 7 and 10), whereas 3D GPR reflections at the same location are quasi-continuous and dip moderately to the northwest. By comparison, footwall seismic reflections A_1 have apparent dips of <10° to the southeast (Figures 7 and 10), which the 3D GPR data indicate are close to true dips. Seismic units A_1 and A_2 are interpreted as fluvial sediments preserved in the accommodation space provided by the repeatedly downthrown side of the Alpine Fault [*McClymont et al.*, 2008]. By implication, these sediments are younger than seismic unit A_3 and may have also overlain this unit on the hanging wall before being subsequently eroded through downcutting of the Maruia River. We interpret the different dip directions of the two units A_1 and A_2 to be a consequence of transpressive folding between the Alpine Fault (AF) and the secondary faults I and II (Figure 10) [*McClymont et al.*, 2009]; sediments in the region represented by seismic unit A_2 are folded and tilted in a general northwest direction.

5.3. Geometry of the Alpine Fault at Shallow Depths

[44] From our data, much of the reverse slip along the Alpine Fault at Calf Paddock appears to be confined to a

single major fault trace. Based on reflection truncations, the fault has an apparent southeasterly dip of 75°–80° from the surface fault scarp through the Quaternary sediments to the offset basement at ~60 m depth.

[45] The dip of the Alpine Fault within the shallow basement is not so well constrained. The moderately steep dipping reflection package X-X′ projects to the basement offset created by the Alpine Fault in Figures 6 and 10. If X-X′ contains fault plane reflections, then the fault would have a distinct listric geometry with dip decreasing from 75°–80° within the Quaternary sediments to ~50° within the basement. The combination of steep dip within the Quaternary sediments to ~60 m depth and shallower dip within the basement is compatible with the borehole-based minimum average 65° dip from the surface to 83 m depth [*Garrick and Hatherton*, 1974].

[46] There are two observations to consider before accepting such a large change in fault dip. First, although the results of finite difference modeling presented in Appendix A demonstrate that X-X′ could indeed contain fault plane reflections, they also demonstrate that X-X′ could be a simple multiple of the basement reflection C_2. Based on the geometry, amplitude, and general character of X-X′, it is not possible to distinguish between these two interpretations. Second, the gentle dips of the layered sediments represented by seismic unit B (best observed in Figure 7) are consistent with a modest decrease in fault plane dip with depth [*Amos et al.*, 2007] or a modest rotation of the fault plane and entire hanging wall over time, but are difficult to reconcile with a significant shallowing of the fault plane below the sediment cover.

[47] In the interpreted seismic section of Figure 10, the maximum fault dip in the basement is a simple depth projection of the 75°–80° dip observed within the Quaternary sediments, whereas the minimum fault dip is defined by the reflection package X-X′. Taking into account the gentle dips of seismic unit B, we speculate that the Alpine Fault continues to have a relatively steep dip within the shallow basement (i.e., close to the dashed line in Figure 10).

5.4. Curvature and Faulting of the Basement Surface on Either Side of the Alpine Fault

[48] There is a notable curvature of the basement surface on either side of the Alpine Fault. This could represent the topography of the prefaulted glacial valley, but the following observations support an interpretation of the characteristic paired convex hanging wall curvature and concave footwall curvature in terms of normal drag generated by the dip-slip component of Alpine Fault displacement [see *Grasemann et al.*, 2005, Figures 1 and 5]: (1) strong changes in reflection characteristics in the region represented by unit A_2 (as seen in the seismic reflection and GPR data) and (2) the prominent faults I and II.

[49] Transpressive forces acting in the region between the Alpine Fault and fault I would have tilted and faulted the shallow sediments, and bending of the footwall would have generated faults I and II.

[50] Small changes in reflection dip and continuity in the hanging wall of the Alpine Fault indicate the presence of other possible subsidiary faults (e.g., dashed lines in Figure 10). The borehole penetrates a steeply dipping crushed zone at 37.5 – 45 m depth within schist bedrock, which has been interpreted as a fault. No information is given on the dip direction of this fault, though its depth coincides with the extension of one of the possible subsidiary fault strands (see intersection of dashed line with the borehole in Figure 10).

5.5. Provisional Dip-Slip Rate Estimation

[51] Significant apparent vertical offset of basement in the seismic profile suggests substantial fault slip since the late Pleistocene. Although quantifying dip-slip rates from vertical offsets of dated horizontal surfaces and known fault dips is clearly possible, estimates are complicated by uncertainties in age, fault dip, original topography, and true offset of the surface. Consequently, we can only provide a provisional estimate of dip-slip rate across the Alpine Fault at Calf Paddock.

[52] We assume that the erosional basement surface dates from the Otira Glaciation (22,000 – 14,000 years ago). Given that the apparent vertical offset in basement is ~35 m and fault dip is 75°–80°, the apparent dip-slip rate at Calf Paddock (estimated using the average values of these parameters) is 2.0 mm/yr with a possible range of 1.6–2.6 mm/yr (estimated from the appropriate upper and lower bounds of these parameters). In presenting this provisional estimate, we recognize that the true vertical offset of the basement surface may differ from the apparent offset due to (1) potential topography of the surface prior to oblique slip and/or (2) normal fault drag and distributed deformation close to the fault. Our provisional dip-slip rate of 2.0 ± 0.6 mm/yr is consistent with the inferred lower slip rates for the northern section of the Alpine Fault [*Berryman et al.*, 1992; *Norris and Cooper*, 2001].

6. Conclusions

[53] We have presented ultrahigh-resolution seismic reflection sections of the Alpine Fault and adjacent regions from the shallow subsurface to ~150 m depth. To obtain high-definition images over this depth range, we designed a general processing sequence that included time-variant spectral whitening, refraction and residual static corrections, F-K filtering, stacking velocity analyses, poststack signal enhancement, and migration. In applying this processing sequence we demonstrated the importance of static corrections at our Calf Paddock study site, where substantial lateral variations in near-surface physical properties exist; a combination of refraction and residual static corrections was necessary to account for distortions of reflections in CMP gathers and avoid generating artificial discontinuities in the stacked and migrated seismic sections. An alternative processing sequence that included surface-consistent deconvolution and dip moveout corrections enhanced the coherency and strength of shallow reflections, in particular a prominent ultrashallow reflection at 3.5–5 m depth.

[54] Our ultrahigh-resolution seismic data contain clear images of the following geological units at successively greater depths: (1) a subhorizontal layer of Holocene sediments abandoned by the Maruia River; (2) dipping late Pleistocene gravel units deposited in various glaciolacustrine fan, alluvial, and glaciofluvial settings; (3) subhorizontal late Pleistocene layered sediments of probable glaciolacustrine origin (only seen in the hanging wall of the Alpine Fault); and (4) the top of the Triassic age

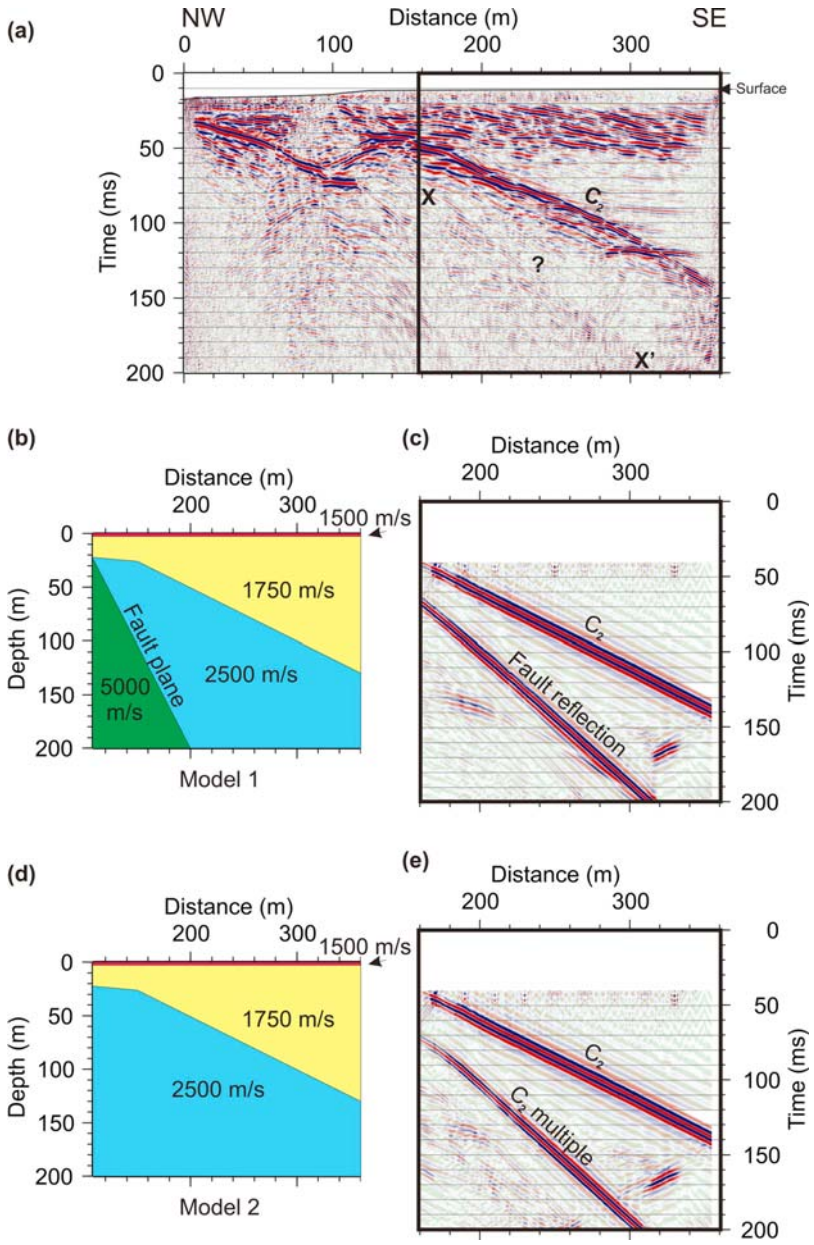

Figure A1. Synthetic modeling of moderately steep dipping energy that projects to the surface trace of the Alpine Fault. (a) Unmigrated section (as in Figure 6a) highlighting the moderately steep dipping energy X-X′. (b) Simple fault plane P wave velocity model 1 used in the finite difference modeling. S wave velocities and densities used in the modeling are defined by the experimentally determined P wave velocities using standard relationships. (c) Resulting stacked synthetic section showing modeled events. (d and e) Same as Figures A1b and A1c, but with model 2 (i.e., uniform velocity across the fault). The multiple of the basement reflection is now clearly seen. Dark blue shading represents positive pulse polarity.

Torlesse schist basement in the hanging wall of the Alpine Fault and Paleozoic age marble basement in the footwall.

[55] The new seismic images provide details on key properties of the Alpine Fault from the surface through the Quaternary sediments into the shallow basement, the top of which is vertically offset ~35 m across the fault in our profile. The Alpine Fault has a steep southeasterly dip of 75°–80° through the sediments, but its dip within the basement is not so tightly constrained. A package of moderately steep dipping quasi-continuous reflections that projects to the basement offset at the Alpine Fault may contain fault plane reflections, indicating a listric shallowing of dip to 50° through basement. Alternatively, the fault dip through basement could be steeper, given that this package of reflections could represent a simple multiple reflection from the dipping basement surface. The subhorizontal

nature of the interpreted glaciolacustrine sediments in the hanging wall favors a smaller change in fault dip with depth. Our preferred interpretation is that the Alpine Fault continues to dip relatively steeply within the shallow basement.

[56] Fault slip appears to be accommodated predominantly on a single fault strand, though significant deformation is observed elsewhere. For example, a marked increase in curvature of the basement surface on either side of the Alpine Fault and strong deformation in the footwall sediments and basement are likely consequences of normal drag created by dip-slip displacements on the fault.

[57] The ~35 m apparent vertical offset of basement across the Alpine Fault together with the estimated age of the eroded basement surface and measured fault dip within the Quaternary sediments yield a provisional dip-slip rate of 2.0 ± 0.6 mm/yr. This provisional dip-slip rate does not account for possible out-of-plane topography on the dated surface or normal drag on this surface close to the fault.

[58] Our 2D ultrahigh-resolution seismic reflection data supply high-quality images of the active Alpine Fault and additional information on fault geometry at depths beyond the reach of GPR surveying and trenching. These are the most vivid shallow seismic images of any continental transform fault zone. Complex fault and deformation structures in the near surface and the dominant, but unknown recent lateral component of slip along the Alpine Fault at Calf Paddock invite the use of 3D seismic reflection studies to further elucidate and refine our interpretations of fault zone deformation.

Appendix A: Moderately Steep Dipping Energy X-X′

[59] The moderately steep dipping reflection package X-X′ on the unmigrated section (Figures 6a and A1a) appears after migration as a suite of ~50° dipping events that projects upwards to the basement offset (Figure 6b). We investigate two plausible explanations for these events. First, we show that X-X′ could contain primary reflections from a moderately steep dipping fault plane given a plausible impedance contrast across the fault. Alternatively, X-X′ could be a simple multiple of the strong basement reflection C_2.

[60] To simulate the two possible scenarios, we have computed synthetic seismograms using *Bohlen*'s [2002] viscoelastic finite difference modeling code. Energy from 10 vertical sources spaced at 20 m intervals was sequentially propagated through the simple velocity models of Figures A1b and A1d and ''recorded'' on 504 hypothetical receivers spaced at 0.5 m intervals along the modeled section of the profile. After simple processing (i.e., bandpass filtering, 60 ms AGC, and velocity analyses), the synthetic CMP-sorted data were stacked. No adjustments to a datum were necessary, because static shifts in the real data (Figure 3d) were generally small (0 ± 1.5 ms) over this section of the profile and thus had negligible effect on the observed traveltimes.

[61] Since we were only interested in traveltime simulations of primary and multiple P wave arrivals (the optimum > 2400 m/s stacking velocity of X-X′ was much greater than that of the primary reflection C_2, precluding X-X′ from being a reflected S wave or P-to-S converted phase), we used (1) a low Q_s value of 3 to attenuate S wave energy, (2) an artificially high weathering layer velocity to avoid numerous near-surface reverberations, and (3) a relatively short 50 ms AGC to equalize the amplitudes of the simulated fault plane reflection and basement multiple in the two stacked sections.

[62] The resultant synthetic stacked sections in Figures A1c and A1e demonstrate that both models are capable of explaining X-X′. A substantial impedance contrast would be required to generate fault plane reflections. Seismic refraction studies at Calf Paddock [*Garrick and Hatherton*, 1974] indicate a velocity contrast between marble (~5000 m/s) on the northwest side of the Alpine Fault and schist (~4000 m/s) on the southeast side. Moreover, fault gouge and highly deformed rock within the fault zone are expected to have anomalously low velocities [*Mooney and Ginzburg*, 1986], and strong weathering of the more vulnerable schist may increase velocity contrasts at shallow depths close to the fault. Generally, a surface multiple would be observed at double the traveltime of a primary reflection on an unmigrated stack. However, our computations demonstrate that a dipping boundary produces a multiple at less than double the traveltime [see also *Telford et al.*, 1990].

[63] Based on the kinematic and dynamic characteristics of X-X′, it is not possible to distinguish between the two explanations. Fortunately, other information contained in the seismic reflection sections (i.e., the gently dipping package of layered reflections B) help resolve this dilemma.

[64] **Acknowledgments.** We thank our hard-working field crew of Wanda Stratford, Chris Grimshaw, Constantin Lazari, Richard Cooksey, Jonas Zolliger, Jaques Ernst, Florian Buech, Scott Barnard, and other students and staff at Canterbury University of New Zealand. We also thank the Editor and reviewers for their helpful comments on this manuscript. The refraction tomography code was developed and provided by Hansruedi Maurer of ETH Zürich and the viscoelastic finite difference modeling code was developed by Thomas Bohlen at the Technical University of Freiberg. This project was funded by ETH Zürich and the Swiss National Science Foundation.

References

Adam, E., B. Milkereit, M. Mareschal, A. E. Barnes, C. Hubert, and M. Salisbury (1992), The application of reflection seismology to the investigation of the geometry of near-surface units and faults in the Blake River Group, Abitibi Belt, Quebec, *Can. J. Earth Sci.*, *29*, 2038–2045.

Amos, C. B., D. W. Burbank, D. C. Nobes, and S. A. L. Read (2007), Geomorphic constraints on listric thrust faulting: Implications for active deformation in the Mackenzie Basin, South Island, New Zealand, *J. Geophys. Res.*, *112*, B03S11, doi:10.1029/2006JB004291.

Berryman, K. R., S. Beanland, A. F. Cooper, H. N. Cutten, R. J. Norris, and P. R. Wood (1992), The Alpine Fault, New Zealand: Variation in Quaternary structural style and geomorphic expression, *Ann. Tectonicae*, *6*, 126–163.

Bohlen, T. (2002), Parallel 3-D viscoelastic finite difference seismic modelling, *Comput. Geosci.*, *28*, 887–899, doi:10.1016/S0098-3004(02)00006-7.

Bradshaw, J. D. (1989), Cretaceous geotectonic patterns in the New Zealand region, *Tectonics*, *8*, 803–820, doi:10.1029/TC008i004p00803.

Büker, F., A. G. Green, and H. Horstmeyer (1998), Shallow seismic reflection study of a glaciated valley, *Geophysics*, *63*, 1395–1407, doi:10.1190/1.1444441.

Canales, L. L. (1984), Random noise reduction, paper presented at 54th Society of Exploration Geophysics Annual Meeting, Atlanta, Ga.

Davey, F. J., T. Henyey, S. Kleffmann, D. Okaya, and D. J. Woodward (1995), Crustal reflections from the Alpine Fault Zone, South Island, New Zealand, *N. Z. J. Geol. Geophys.*, *38*, 601–604.

DeMets, C., R. G. Gordon, D. F. Argus, and S. Stein (1994), Effect of recent revisions to the geomagnetic reversal time scale on estimates of current plate motions, *Geophys. Res. Lett.*, *21*, 2191–2194, doi:10.1029/94GL02118.

Garrick, R. A., and T. Hatherton (1974), Seismic refraction profiles across the Alpine Fault, *Rep. 87*, 41 pp., Geophys. Div., Dep. of Sci. and Ind. Res., Wellington, New Zealand.

Gazdag, J. (1978), Wave equation migration with the phase-shift method, *Geophysics*, *43*, 1342–1351, doi:10.1190/1.1440899.

Grasemann, B., S. Martel, and C. Passchier (2005), Reverse and normal drag along a fault, *J. Struct. Geol.*, *27*, 999–1010, doi:10.1016/j.jsg.2005.04.006.

Hole, J. A., R. D. Catchings, K. C. St. Clair, M. J. Rymer, D. A. Okaya, and B. J. Carney (2001), Steep-dip seismic imaging of the shallow San Andreas Fault near Parkfield, *Science*, *294*, 1513–1515, doi:10.1126/science.1065100.

Improta, L., and P. P. Bruno (2007), Combining seismic reflection with multifold wide-aperture profiling: An effective strategy for high-resolution shallow imaging of active faults, *Geophys. Res. Lett.*, *34*, L20310, doi:10.1029/2007GL031893.

Jakubowicz, H. (1990), A simple efficient method of dip-moveout correction, *Geophys. Prospect.*, *38*, 221–245, doi:10.1111/j.1365-2478.1990.tb01843.x.

Kleffmann, S., F. J. Davey, A. Melhuish, D. Okaya, and T. Stern (1998), Crustal structure in the central South Island, New Zealand, from the Lake Pukaki seismic experiment, *N. Z. J. Geol. Geophys.*, *41*, 39–49.

Langridge, R., and K. R. Berryman (2005), Morphology and slip rate of the Hurunui section of the Hope Fault, South Island, New Zealand, *N. Z. J. Geol. Geophys.*, *48*, 43–57.

Lanz, E., H. Maurer, and A. G. Green (1998), Refraction tomography over a buried waste disposal site, *Geophysics*, *63*, 1414–1433, doi:10.1190/1.1444443.

Lawton, D. C. (1989), Computation of refraction static corrections using first-break traveltime differences, *Geophysics*, *54*, 1289–1296, doi:10.1190/1.1442588.

Lemiszki, P. J., and L. D. Brown (1988), Variable crustal structure of strike-slip fault zones as observed on deep seismic reflection profiles, *Geol. Soc. Am. Bull.*, *100*, 665–676, doi:10.1130/0016-7606(1988)100<0665:VCSOSS>2.3.CO;2.

Levin, S. A. (1989), Surface-consistent deconvolution, *Geophysics*, *54*, 1123–1133, doi:10.1190/1.1442747.

Mabin, M. C. G. (1983), The late Pleistocene glacial sequence in the middle Maruia valley, southeast Nelson, New Zealand, *N. Z. J. Geol. Geophys.*, *26*, 85–96.

McBride, J. H., and W. J. Nelson (2001), Seismic reflection images of shallow faulting, northernmost Mississippi Embayment, north of the New Madrid Seismic Zone, *Bull. Seismol. Soc. Am.*, *91*, 128–139, doi:10.1785/0120000039.

McClymont, A., A. G. Green, R. Streich, H. Horstmeyer, J. Tronicke, D. C. Nobes, J. R. Pettinga, J. Campbell, and R. Langridge (2008), Visualization of active faults using geometric attributes of 3D GPR data: An example from the Alpine fault zone, New Zealand, *Geophysics*, *73*, B11–B23, doi:10.1190/1.2825408.

McClymont, A., A. G. Green, A. Kaiser, H. Horstmeyer, and R. Langridge (2009), Shallow fault segmentation of the Alpine fault zone, New Zealand revealed from 2- and 3-D GPR surveying, *J. Appl. Geophys.*, doi:10.1016/j.appgeo.2009.08.003, in press.

Mooney, W. D., and A. Ginzburg (1986), Seismic measurements of the internal properties of fault zones, *Pure Appl. Geophys.*, *124*, 141–157, doi:10.1007/BF00875723.

Nathan, S., M. S. Rattenbury, and R. P. Suggate (2002), Geology of the Greymouth area, *Geol. Map 12*, scale 1:250,000, Inst. of Geol. and Nucl. Sci., Lower Hutt, New Zealand.

Norris, R. J., and A. F. Cooper (1995), Origin of small-scale segmentation and transpressional thrusting along the Alpine fault, New Zealand, *Geol. Soc. Am. Bull.*, *107*, 231–240, doi:10.1130/0016-7606(1995)107<0231:OOSSSA>2.3.CO;2.

Norris, R. J., and A. F. Cooper (2001), Late Quaternary slip rates and slip partitioning on the Alpine Fault, New Zealand, *J. Struct. Geol.*, *23*, 507–520, doi:10.1016/S0191-8141(00)00122-X.

Norris, R. J., and A. F. Cooper (2007), The Alpine Fault, New Zealand; surface geology and field relationships, in *A Continental Plate Boundary: Tectonics at South Island, New Zealand*, *Geophys. Monogr. Ser*, vol. 175, edited by D. Okaya et al., pp. 157–175, AGU, Washington, D. C.

Okaya, D., T. Stern, F. J. Davey, S. Henrys, and S. Cox (2007), Continent-Continent collision at the Pacific/Indo-Australian plate boundary: Background, motivation, and principal results, in *A Continental Plate Boundary: Tectonics at South Island, New Zealand*, *Geophys. Monogr. Ser*, vol. 175, edited by D. Okaya et al., pp. 1–18, AGU, Washington, D. C.

Pratt, T. L., J. F. Dolan, J. K. Odum, W. J. Stephenson, R. A. Williams, and M. E. Templeton (1998), Multiscale seismic imaging of active fault zones for hazard assessment: A case study of the Santa Monica fault zone, Los Angeles, California, *Geophysics*, *63*, 479–489, doi:10.1190/1.1444349.

Robertsson, J. O. A., K. Holliger, A. G. Green, A. Pugin, and R. De Iaco (1996), Effects of near-surface waveguides on shallow high-resolution seismic refraction and reflection data, *Geophys. Res. Lett.*, *23*, 495–498, doi:10.1029/96GL00384.

Ronen, J., and J. F. Claerbout (1985), Surface-consistent residual statics estimation by stack-power maximization, *Geophysics*, *50*, 2759–2767, doi:10.1190/1.1441896.

Schmelzbach, C., A. G. Green, and H. Horstmeyer (2005), Ultra-shallow seismic reflection imaging in a region characterized by high source-generated noise, *Near Surf. Geophys.*, *3*, 33–46, doi:10.3997/1873-0604.2004027.

Steeples, D. W., A. G. Green, T. V. McEvilly, R. D. Miller, W. E. Doll, and J. W. Rector (1997), A workshop examination of shallow seismic reflection surveying, *Lead. Edge*, *16*, 1641–1647, doi:10.1190/1.1437543.

Stern, T. A., and J. H. McBride (1998), Seismic exploration of continental strike-slip zones, *Tectonophysics*, *286*, 63–78, doi:10.1016/S0040-1951(97)00255-2.

Suggate, R. P. (1965), Late Pleistocene geology of the northern part of the South Island, New Zealand, *Bull. 77*, 87 pp., N. Z. Geol. Surv., N. Z. Dep. of Sci. and Ind. Res., Lower Hutt.

Suggate, R. P. (1990), Late Pliocene and Quaternary glaciations of New Zealand, *Quat. Sci. Rev.*, *9*, 175–197, doi:10.1016/0277-3791(90)90017-5.

Sutherland, R., K. R. Berryman, and R. J. Norris (2006), Quaternary slip rate and geomorphology of the Alpine fault: Implications for kinematics and seismic hazard in southwest New Zealand, *Geol. Soc. Am. Bull.*, *118*, 464–474, doi:10.1130/B25627.1.

Sutherland, R., et al. (2007), Do great earthquakes occur on the Alpine fault in central South Island, New Zealand? in *A Continental Plate Boundary: Tectonics at South Island, New Zealand*, *Geophys. Monogr. Ser*, vol. 175, edited by D. Okaya et al., pp. 235–251, AGU, Washington, D. C.

Telford, W. M., L. P. Geldart, and R. E. Sheriff (1990), *Applied Geophysics*, 2nd ed., 770 pp., Cambridge Univ. Press, New York.

Wellman, H. W. (1952), The Alpine Fault in detail: River terrace displacement, Maruia River, *N. Z. J. Sci. Technol.*, *B33*, 409–414.

Yetton, M. D. (2002), Paleoseismic investigation of the North and West Wairau sections of the Alpine Fault, South Island, New Zealand, *Rep. 99/353*, 96 pp., Earthquake Comm. Res. Found., Christchurch, New Zealand.

Yilmaz, O. (2001), *Seismic Data Analysis: Processing, Inversion, and Interpretation of Seismic Data*, 2027 pp., Soc. of Explor. Geophys., Tulsa, Okla.

F. M. Campbell, A. G. Green, H. Horstmeyer, A. E. Kaiser, and E. Manukyan, Institute of Geophysics, Department of Earth Sciences, ETH Zürich, Sonneggstrasse 5, CH-8092, Zürich, Switzerland. (kaiseran@aug.ig.erdw.ethz.ch)

M. Finnemore and D. C. Nobes, Department of Geological Sciences, University of Canterbury, Christchurch 8140, New Zealand.

R. M. Langridge, GNS Science, 1 Fairway Drive, Avalon, Lower Hutt 5010, New Zealand.

N. Mancktelow, Geological Institute, Department of Earth Sciences, ETH Zürich, Sonneggstrasse 5, CH-8092, Zürich, Switzerland.

A. F. McClymont, Department of Geoscience, University of Calgary, 2500 University Dr. NW, Calgary, AB T2N 1N4, Canada.